

## Supplementary Information

### Photon-induced isomerization enables high-performance polymer solar cells

Hanzhi Wu,<sup>a</sup> Jiawei Qiao,<sup>a</sup> Jinqun Xu,<sup>a</sup> Mingxu Zhou,<sup>a</sup> Zhen Fu,<sup>a</sup> Peng Lu,<sup>b</sup> Hang Yin,<sup>a</sup> Xiaoyan Du,<sup>a</sup> Wei Qin,<sup>a</sup> Kangning Zhang<sup>\*a</sup> and Xiaotao Hao<sup>\*ac</sup>

<sup>a</sup>School of Physics, State Key Laboratory of Crystal Materials, Shandong University, Jinan, Shandong 250100, P. R. China.

<sup>b</sup>School of Physics, National Demonstration Center for Experimental Physics Education, Shandong University, Jinan, Shandong 250100, P. R. China

<sup>c</sup>School of Chemistry, The University of Melbourne, Parkville, Victoria 3010, Australia

E-mail: zhangkn@sdu.edu.cn (K.N.Z); haoxt@sdu.edu.cn (X.T.H).

#### 1. Experimental Section

##### 1.1. Full Names of the Used OPV Materials

PM6: Poly[(2,6-(4,8-bis(5-(2-ethylhexyl-3-fluoro)thiophen-2-yl)-benzo[1,2-b:4,5-b'] dithiophene))-alt-(5,5-(1',3'-di-2-thienyl-5',7'-bis(2-ethylhexyl)benzo[1',2'-c:4',5'-c'] dithiophene-4,8-dione)]

PY-IT: (Poly[(2,2'-((2Z,2'Z)-((12,13-bis(2-octyldodecyl)-3,9-diundecyl-12,13-dihydro[1,2,5] thiadiazolo[3,4e]thieno[2'',3'':4',5'])thieno[2',3':4,5]pyrrolo[3,2-g]thieno[2',3':4,5]thieno[3,2-b]-indole-2,10-diyl)bis(methanylylidene))bis(5-methyl-3-oxo-2,3-dihydro-1H-indene-2,1-diylidene)) dimalononitrile-co-2,5-thiophene)

##### 1.2. Materials

PM6 (Mn = 47.7 kDa, PDI = 2.39), PY-IT (Mn = 5.7 kDa, PDI = 2.13), and PDINN were purchased from Solarmer Materials (Beijing) Inc. PEDOT:PSS (Clevios PVP Al 4083) aqueous solution was purchased from Xi'an Yuri Solar Co., Ltd. Chloroform (CF), methanol and 1-chloronaphthalene (1-CN) were purchased from Sigma-Aldrich Inc. Indium tin oxide (ITO) substrates (16.1×16.1 mm<sup>2</sup>) were purchased from Advanced Election Technology Co.,Ltd. Unless otherwise stated, all chemicals and solvents were of reagent grade and used as received.

##### 1.3. Process of UV laser irradiation

7 mg/ml of PM6 was bottled in a 1.5 ml glass vial (with transmittance over 90% for the incident

UV-laser) with a magnetic stir bar. After the full dissolving of PM6 in CF at 45 °C for 2 h, the vial was irradiated by a UV solid-state laser (5 mW cm<sup>-2</sup>, 360 nm) for 10 min. At the same time, the PM6 solution was gently stirred at 200 rpm. 8.4 mg/ml of PY-IT CF solution was subjected to the same treatment protocol.

#### 1.4. Fabrication of the devices

The conventional organic photovoltaic (OPV) devices with an ITO/PEDOT:PSS/Active layer/PDINN/Ag structure were fabricated using the following procedure. Patterned ITO substrates ( $R_{\text{sheet}} = 15 \Omega$  per square) were cleaned in sequence in detergent, deionized water, acetone, and isopropanol in an ultrasonic bath for 20 min respectively. Then, the ITO substrates were treated by ultraviolet–ozone for 20 min. PEDOT:PSS solution (PEDOT:PSS:deionized water is 1:1) was spin cast onto ITO with 4000 rpm for 60 s to as the hole transportation layer, followed by annealing at 150 °C for 15 min in the air. For all devices, the active layers were formed by spin coating a chloroform solution of active layer in a N<sub>2</sub>-filled glove box. The total D/A weight ratio was kept at 1:1.2 in devices. The preparation of the LBL active layer involves spin-coating the PM6 layer (in CF) on the PEDOT:PSS layer and then depositing the PY-IT layer (in CF with 2% 1-CN solvent additives). Assisted by the swelling of PM6 by a CF solution, penetration of PY-IT into the PM6 layer induces the LBL device architecture. Subsequently, the films were annealed under 100 °C for 10 min. After the annealing, PDINN methanol solution (1.5 mg mL<sup>-1</sup>) was spin-coated onto the active layers at 3000 rpm. Then, Ag cathode (100 nm) was evaporated on the electronic transport layer at a high vacuum of  $1 \times 10^{-4}$  Pa.

The inverted solar cells with an ITO/ZnO/active layer/ MoO<sub>3</sub>/Ag structure were fabricated as well. The precursor solution of ZnO was spin-coated on the patterned ITO substrates at 4000 rpm for 50 s and baked at 70 °C for 10 min in glovebox with nitrogen atmosphere. Subsequently, the ZnO layers were further thermally annealed at 150 °C for 30 min under ambient conditions. An 8 nm MoO<sub>3</sub> layer was thermally evaporated on the top of the active layers. Moreover, for single-carrier device fabrication, the hole-only and electron-only devices were fabricated with a structure of ITO/PEDOT:PSS/active layer/MoO<sub>3</sub>/Ag or ITO/ZnO/active layer/PDINN/Ag, respectively.

#### 1.5. Measurements of OPV Devices

The  $J$ – $V$  measurements were performed under AM 1.5 G (100 mW cm<sup>-2</sup>) using a 3 A solar simulator (Sofn Instruments Co., Ltd) in an N<sub>2</sub>-filled glove box at room temperature combining

with a computer-controlled Keithley 2400 source. The light intensity was calibrated using a standard monosilicon reference cell. The scanning range is from -1.0 V to 1.0 V. The external quantum efficiency (EQE) spectra were obtained with the 7-SCSpec test system calibrated by a standard Si diode. Thermal stability measurements of the devices were performed on a hot plate under continuous thermal annealing at 80 °C in a N<sub>2</sub>-filled glovebox. Photostability measurements of the devices were conducted under continuous illumination of the simulated intensity of 100 mW cm<sup>-2</sup> using a white light LED array. The frequency-dependent capacitance spectra were achieved by an impedance spectroscopy. The FTPS-EQE was recorded by PECT-600 Fourier-transform photocurrent spectroscopy. Transient photocurrent (TPC) and transient photovoltage (TPV) measurements were performed via an integrated equipment called *Paivos*.

## 1.6. Characterizations

<sup>1</sup>H NMR spectra were recorded on a Bruker Advance III (600 MHz for <sup>1</sup>H NMR). UV-Vis absorption spectra were measured by a UV-Vis-NIR spectrophotometer (Cary 5000, Agilent Technologies, Inc.) under ambient conditions. The GIWAXS data were obtained at Shanghai Synchrotron Radiation Facility (BL16B1). Temperature-dependent photoluminescence (PL) spectra measurements for the encapsulated films were performed through a spectrometer (PG2000 Pro, Fuxiang Inc.) from the integrated fluorescence lifetime imaging microscopy (FLIM). A Ti:sapphire amplifier (Astrella, Coherent) supplies 800 nm pulse to excite the encapsulated films and create the PL signals. The liquid nitrogen cooling chamber (TC280, East Changing, Inc.) was employed to modulate the target temperature. The measurements of femtosecond transient absorption spectra were conducted with an optical instrument consisting of a Ti:sapphire femtosecond laser (coherent) and an optical parametric amplifier (OPA) system. Then the 800 nm pulse was separated into two parts by a beam splitter. One part was coupled into an optical parametric amplifier (TOPAS, Coherent) to generate the pump pulses at 600 nm. The other part was focused onto a sapphire plate and a YAG plate to generate white light supercontinuum as the probe beams with spectra covering 750-1600 nm. The seed pulses were split into two parts of laser, one for routing to the OPA to provide a 400 and 750 nm pump pulse that were used in this work and the other for generating a broad band of 520-800 nm (visible) and 850-1300 nm (NIR) probe light. Xenon lamps were used as light sources to obtain the in-situ transmission absorption spectrum from the Maya2000 Pro (Ocean Insight) spectrometer for the spin-coating process. The film-depth-dependent light absorption spectroscopy was acquired upon a film-depth-dependent light absorption spectrometer (PU100, Puguangweishi Co. Ltd). In-situ soft plasma etching at low pressure (less than 20 Pa) was used

to extract the depth-resolved absorption spectrum for the active layers. The Beer-Lambert's law was utilized to fit the FLAS results, which were subsequently used to fit the exciton generation contour upon a modified optical matrix-transfer approach.

### 1.7. Energy Loss Measurement

The energy loss of OSCs was determined according to the following equation<sup>1,2</sup> of  $E_{loss} = E_g - qV_{OC} = (E_g - qV_{OC}^{rad}) + (qV_{OC}^{rad} - qV_{OC})$

where  $E_g$  is the band gap and  $V_{OC}^{rad}$  is the  $V_{OC}$  when only considering radiative recombination with realistic absorption edges. When all recombination is radiative, the related radiative limit  $V_{OC}^{rad}$  was calculated according to the following equation given by

$$V_{OC}^{rad} = \frac{kT}{q} \ln \left( \frac{J_{SC}}{J_0^{rad}} + 1 \right) = \frac{kT}{q} \ln \left( \frac{q \int_0^{\infty} EQE_{PV}(E) \cdot \Phi_{AM1.5}(E) dE}{q \int_0^{\infty} EQE_{PV}(E) \cdot \Phi_{BB}(E) dE} + 1 \right)$$

herein,  $J_0^{rad}$  is the saturated current density for radiative recombination,  $\Phi_{BB}(E)$  is the blackbody spectrum with the following expression as below,

$$\phi_{BB}(E) = \frac{2\pi E^2}{h^3 c^2} \exp\left(-\frac{E}{kT}\right)$$

where  $h$  is the Planck's constant and  $c$  is the light speed in a vacuum. Moreover, the nonradiative voltage loss ( $V_{OC}^{nonrad}$ ) was quantified through<sup>1,2</sup>

$$V_{OC}^{nonrad} = V_{OC}^{rad} - V_{OC}$$

As for the band gap of the actual OPV devices ( $E_g^{PV}$ ), it was obtained from the FTES-EQE spectrum described by<sup>3</sup>

$$E_g^{PV} = \frac{\int_a^b E \cdot P(E) \cdot dE}{\int_a^b P(E) \cdot dE}$$

where  $P(E)$  is the distribution of the calculated band gap ( $P(E) = dEQE/dE$ ). Especially, the integral boundaries ( $a, b$ ) were selected where  $P(a) = P(b) = 0.5 \max[P(E)]$ .

### 1.8. Computational Methods and Details

Density functional theory simulations were carried out using Gaussian 09 software. Single molecule was modeled in the gas phase at the B3LYP level of theory with the basis set 6-

311G(d,p). For frequency calculations, alkyl side chains were simplified to methyl groups to reduce computational time. Structures were optimized to a local minimum energy conformation, with frozen dihedral angles used to simulate the change in molecular conformation. Calculated frequencies were corrected using an empirical factor of 0.97 for the frequency of vibration.

## 2. Supplementary Figures

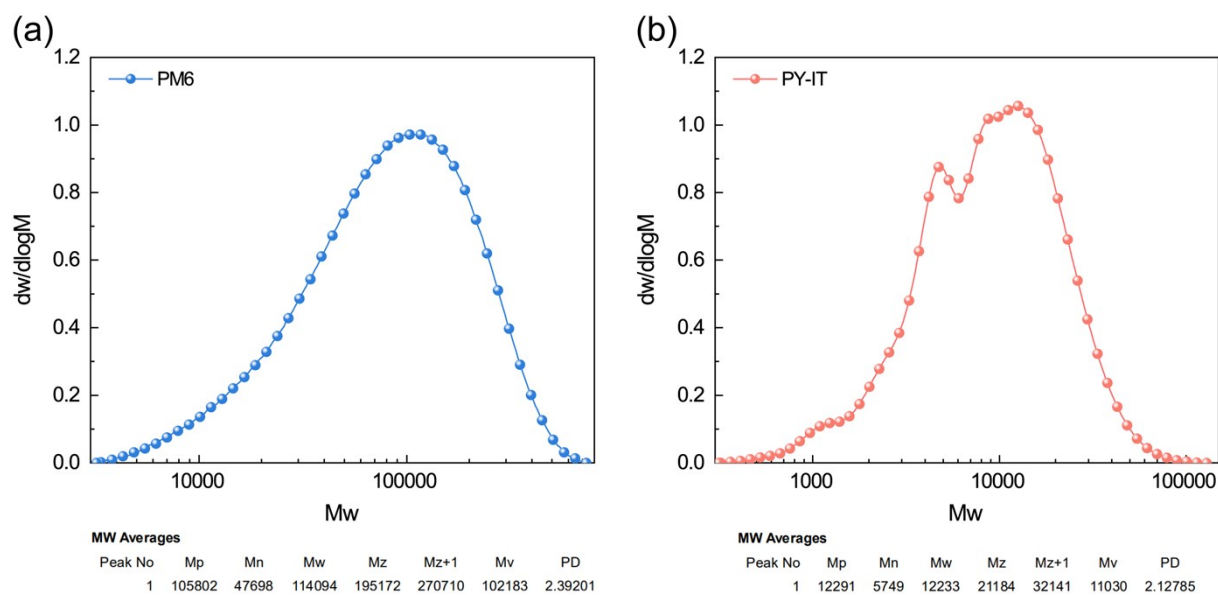


**Figure S1.** Gel permeation chromatography (GPC) curves of (a) PM6 and (b) PY-IT.

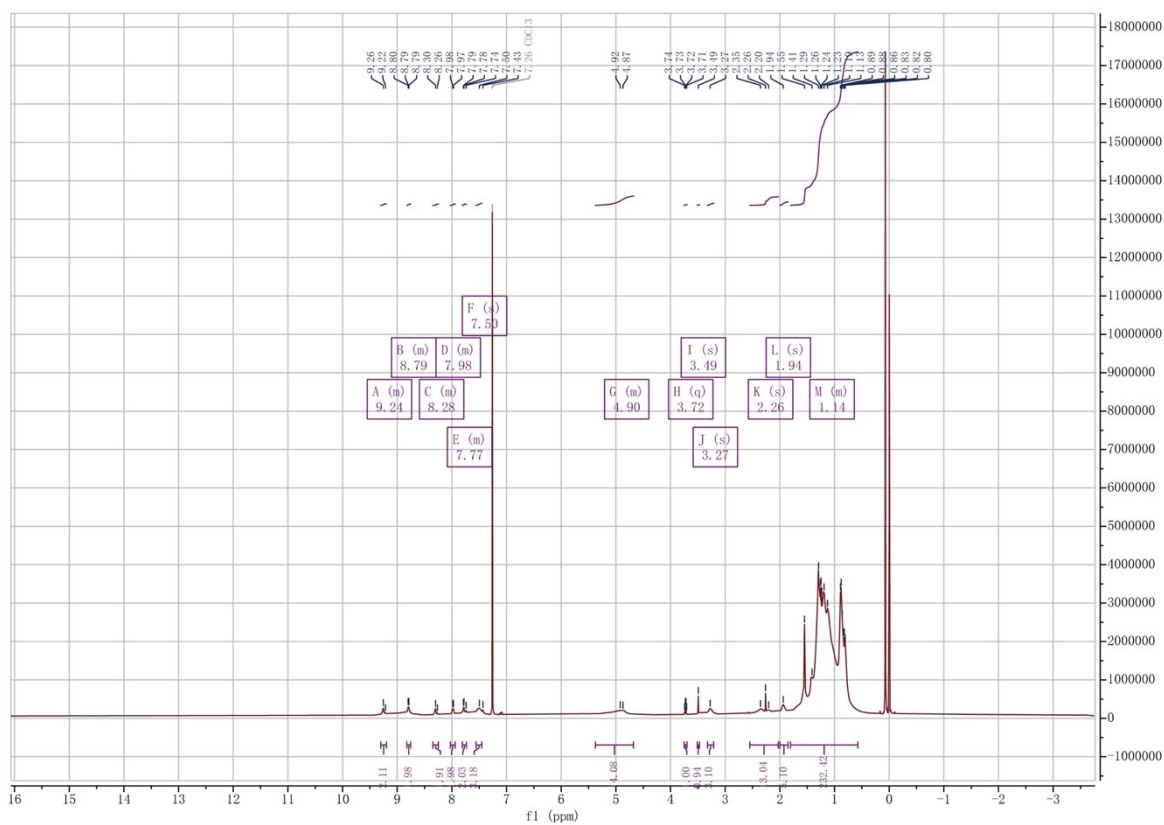


**Figure S2.**  $^1\text{H}$  NMR spectrum of pristine PY-IT in  $\text{CDCl}_3$ .



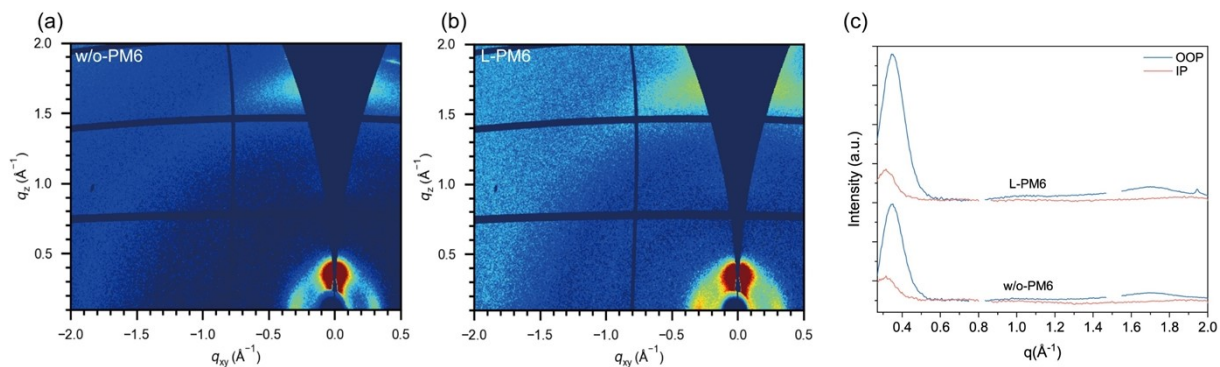


**Figure S5.** 2D GIWAXS patterns of (a) pristine PM6 (w/o-PM6) and (b) L-PM6 neat films. (c) The extracted 1D line-cut profiles from the corresponding neat films.

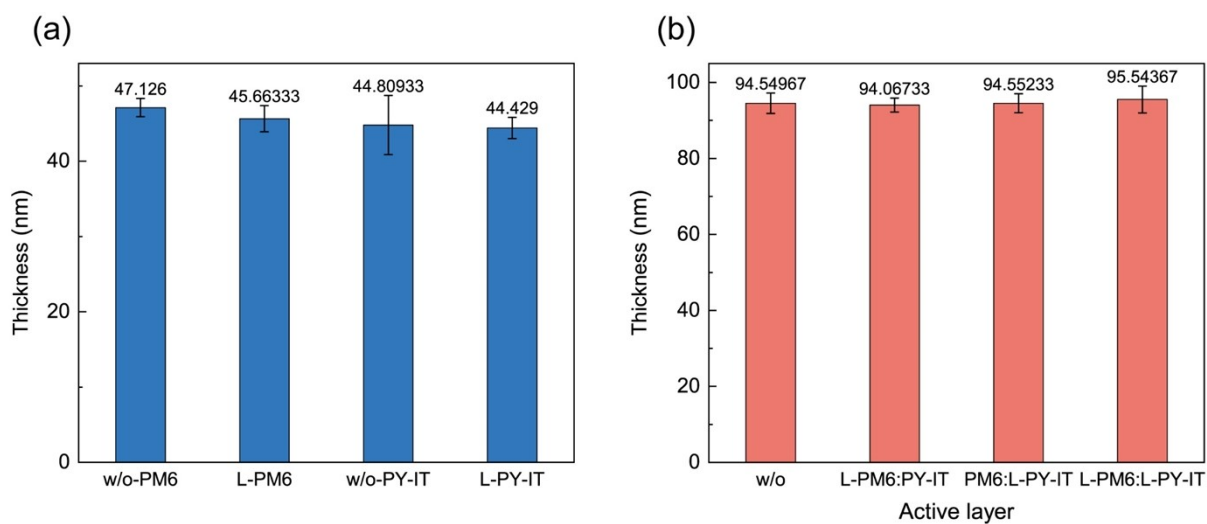


**Figure S6.** Thicknesses of (a) four neat films and (b) four blend films.

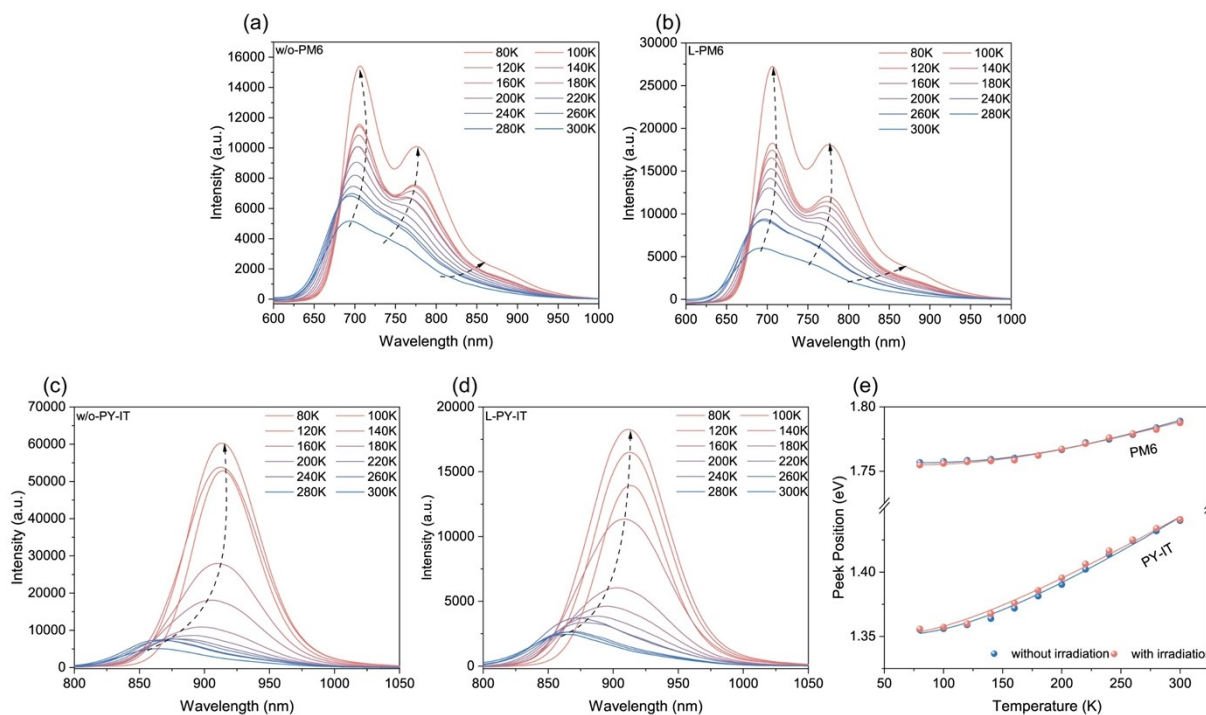


**Figure S7.** Photoluminescence spectra of (a) w/o-PM6, (b) L-PM6, (c) w/o-PY-IT, and (d) L-PY-IT neat films at selected temperatures. (e) Peak position of the  $\pi$ -EXs emission peak as a function of temperature in the corresponding films.

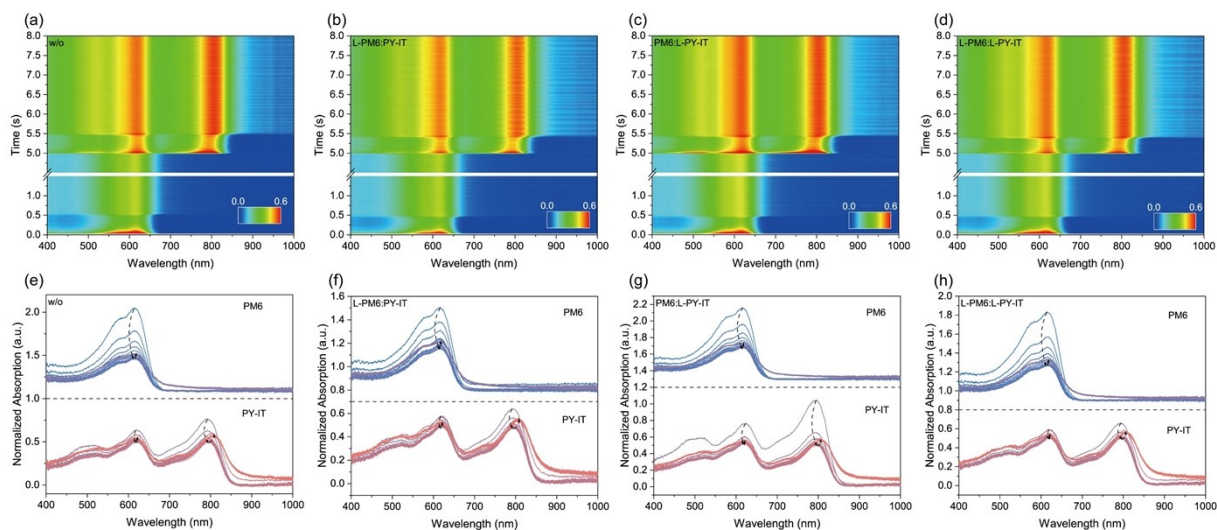


**Figure S8.** Time-dependent contour maps of UV-vis absorption spectra changes for (a) w/o, (b) L-PM6:PY-IT, (c) PM6:L-PY-IT, and (d) L-PM6:L-PY-IT systems during spin-coating processes. Corresponding 1D spectra for (e) w/o, (f) L-PM6:PY-IT, (g) PM6:L-PY-IT, and (h) L-PM6:L-PY-IT systems during spin-coating processes.

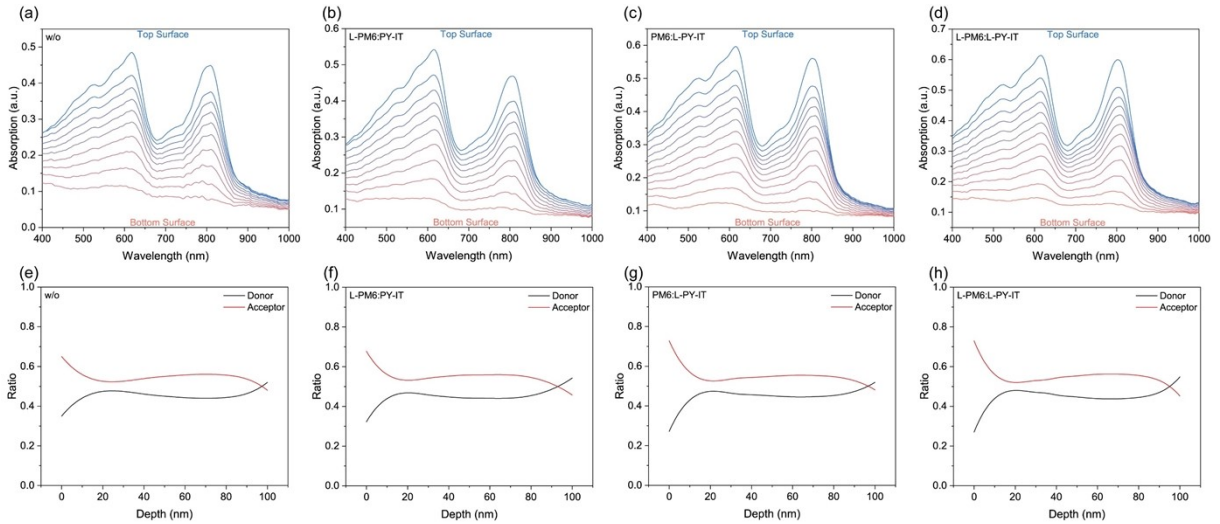


**Figure S9.** Film-depth-dependent light absorption spectra of (a) w/o, (b) L-PM6:PY-IT, (c) PM6:L-PY-IT, and (d) L-PM6:L-PY-IT blend films. Corresponding film-depth-dependent composition profiles for (e) w/o, (f) L-PM6:PY-IT, (g) PM6:L-PY-IT, and (h) L-PM6:L-PY-IT blend films.

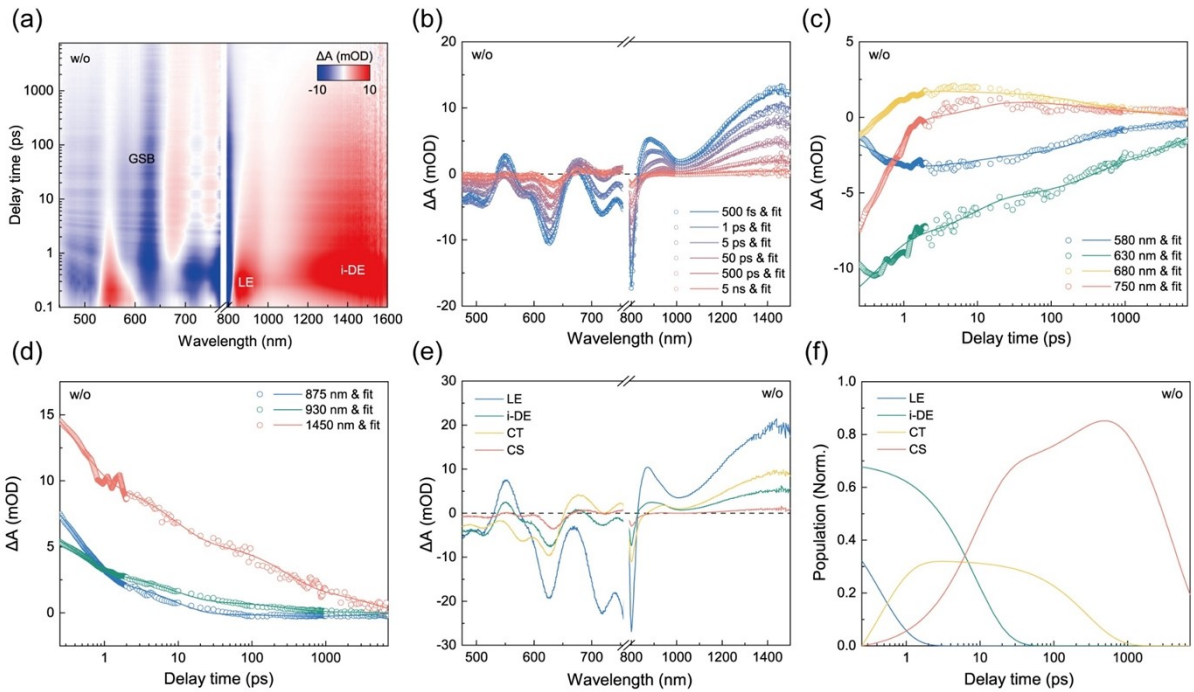


**Figure S10.** (a) 2D color plots of TA data of control blend films at different delay times. (b) Raw TA spectral data and their corresponding fitted spectra at different delay times. Decay dynamics probed at (c) 580, 630, 680, 750 nm, and (d) 875, 930, 1450 nm with their corresponding fitting results. (e) Spectral contribution and (f) temporal evolution of LEs, i-DEs, CTs and CSs.

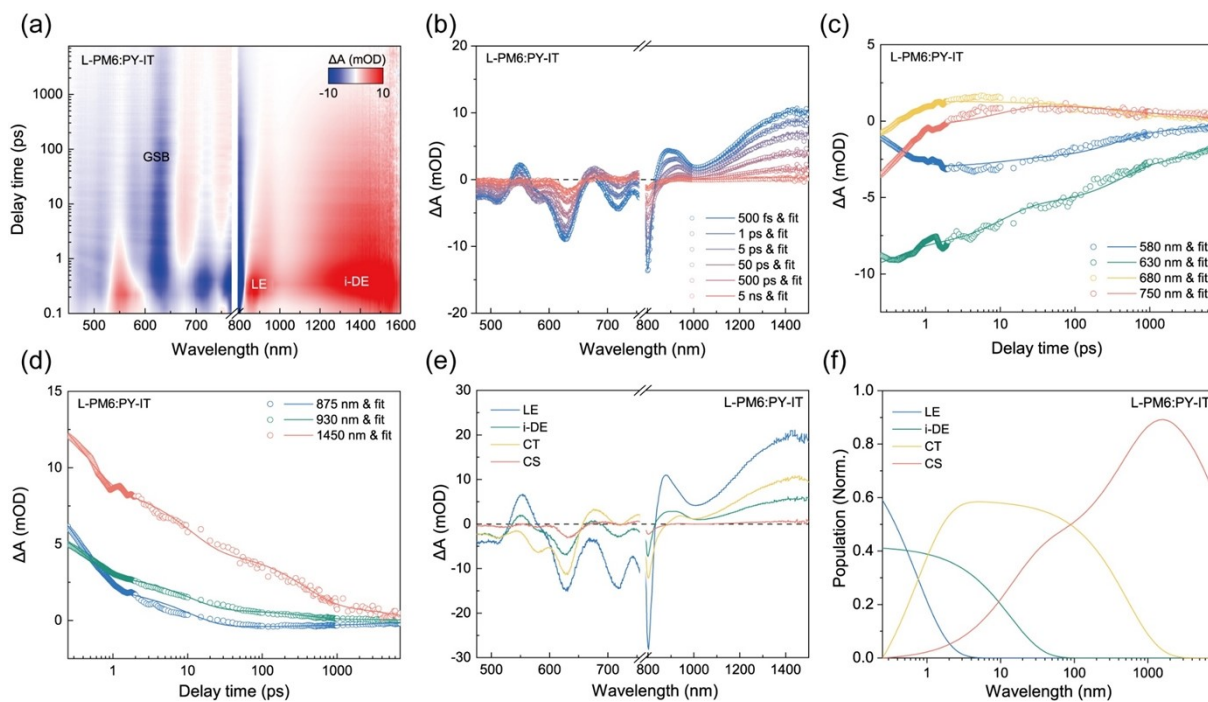


**Figure S11.** (a) 2D color plots of TA data of L-PM6:PY-IT blend films at different delay times. (b) Raw TA spectral data and their corresponding fitted spectra at different delay times. Decay dynamics probed at (c) 580, 630, 680, 750 nm, and (d) 875, 930, 1450 nm with their corresponding fitting results. (e) Spectral contribution and (f) temporal evolution of LEs, i-DEs, CTs and CSs.

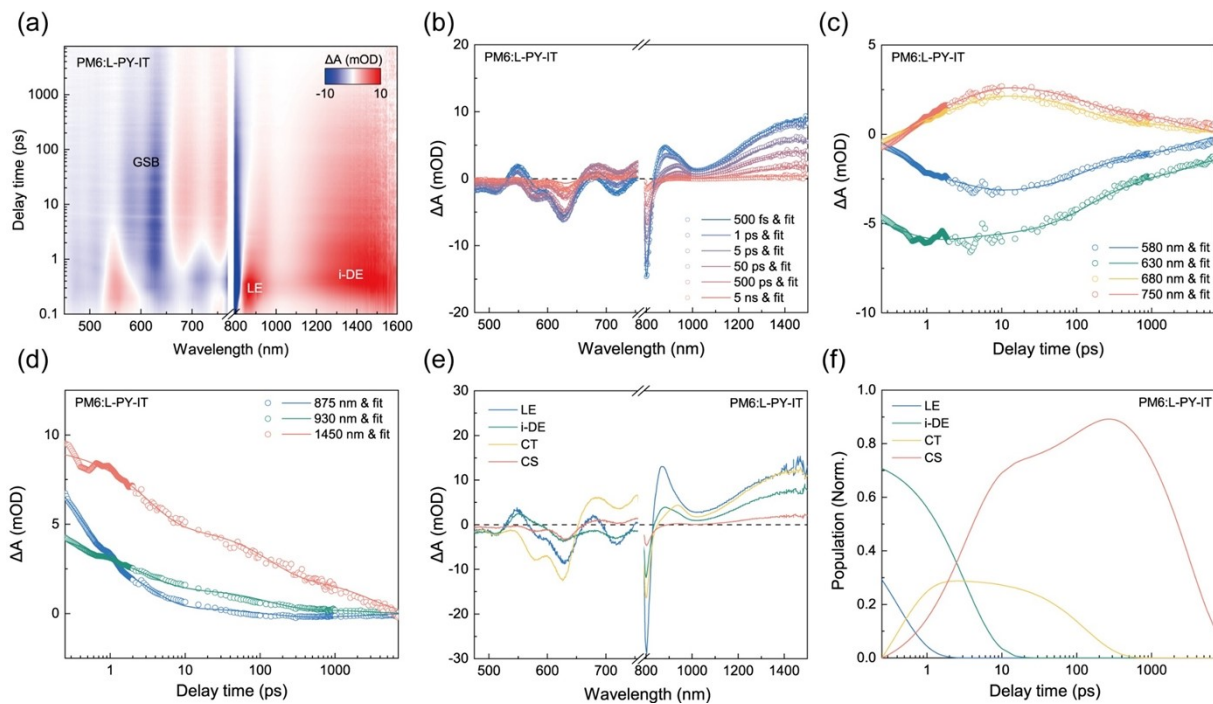


**Figure S12.** (a) 2D color plots of TA data of PM6:L-PY-IT blend films at different delay times. (b) Raw TA spectral data and their corresponding fitted spectra at different delay times. Decay dynamics probed at (c) 580, 630, 680, 750 nm, and (d) 875, 930, 1450 nm with their corresponding fitting results. (e) Spectral contribution and (f) temporal evolution of LEs, i-DEs, CTs and CSs.

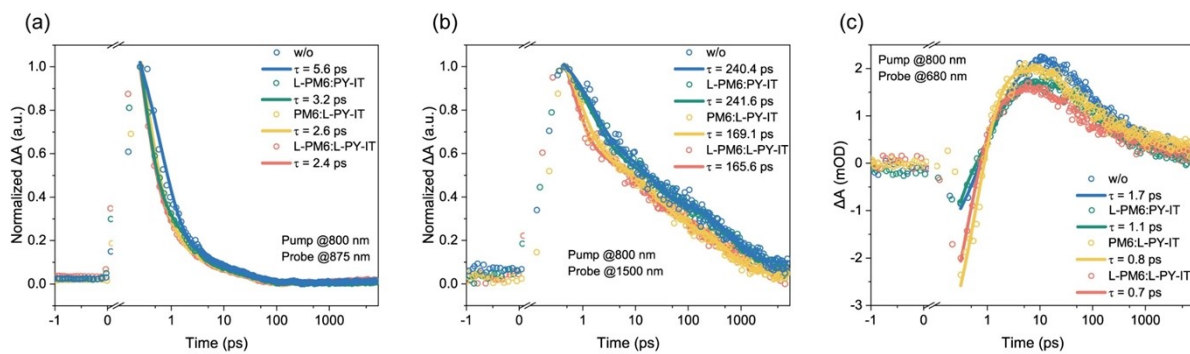


**Figure S13.** Decay dynamics probed at (a) 875 nm, (b) 1500 nm, and (c) 680 nm from four different PM6:PY-IT blend films.

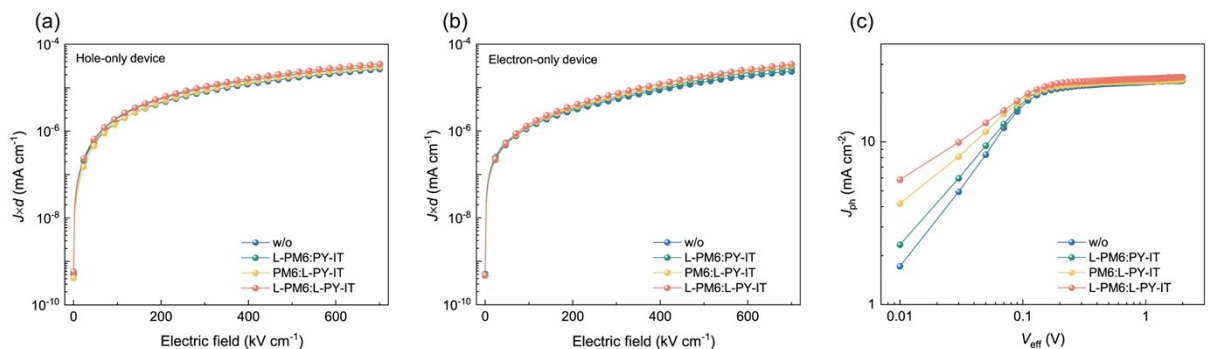


**Figure S14.**  $J \times d$  as a function of the applied electric field for (a) hole-only and (b) electron-only four different devices. (c)  $J_{ph}$ - $V_{eff}$  curves of four different devices.

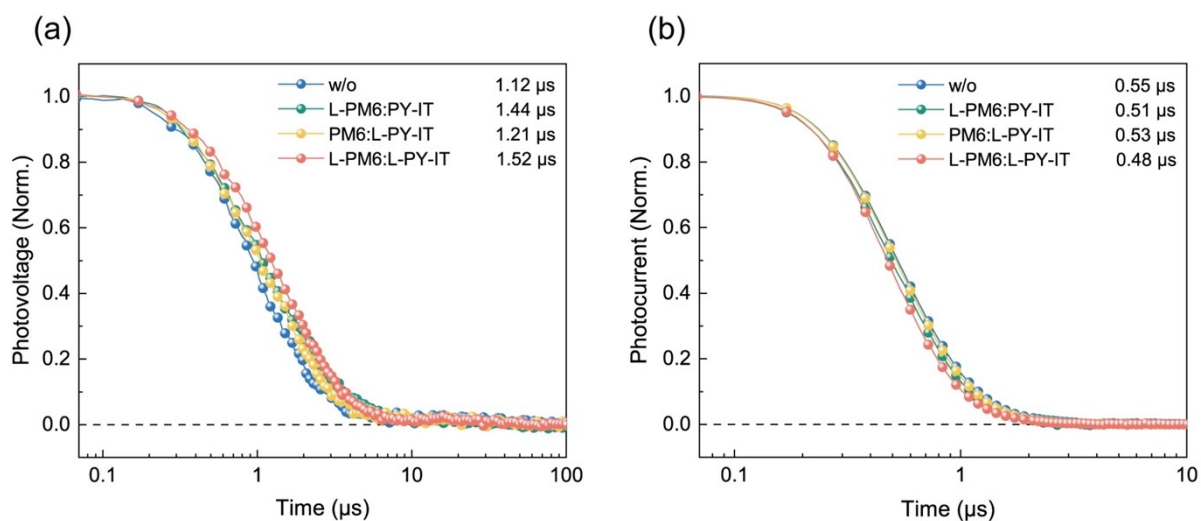


**Figure S15.** (a) Transient photovoltage (TPV) and (b) transient photocurrent (TPC) decay curves of four different devices.

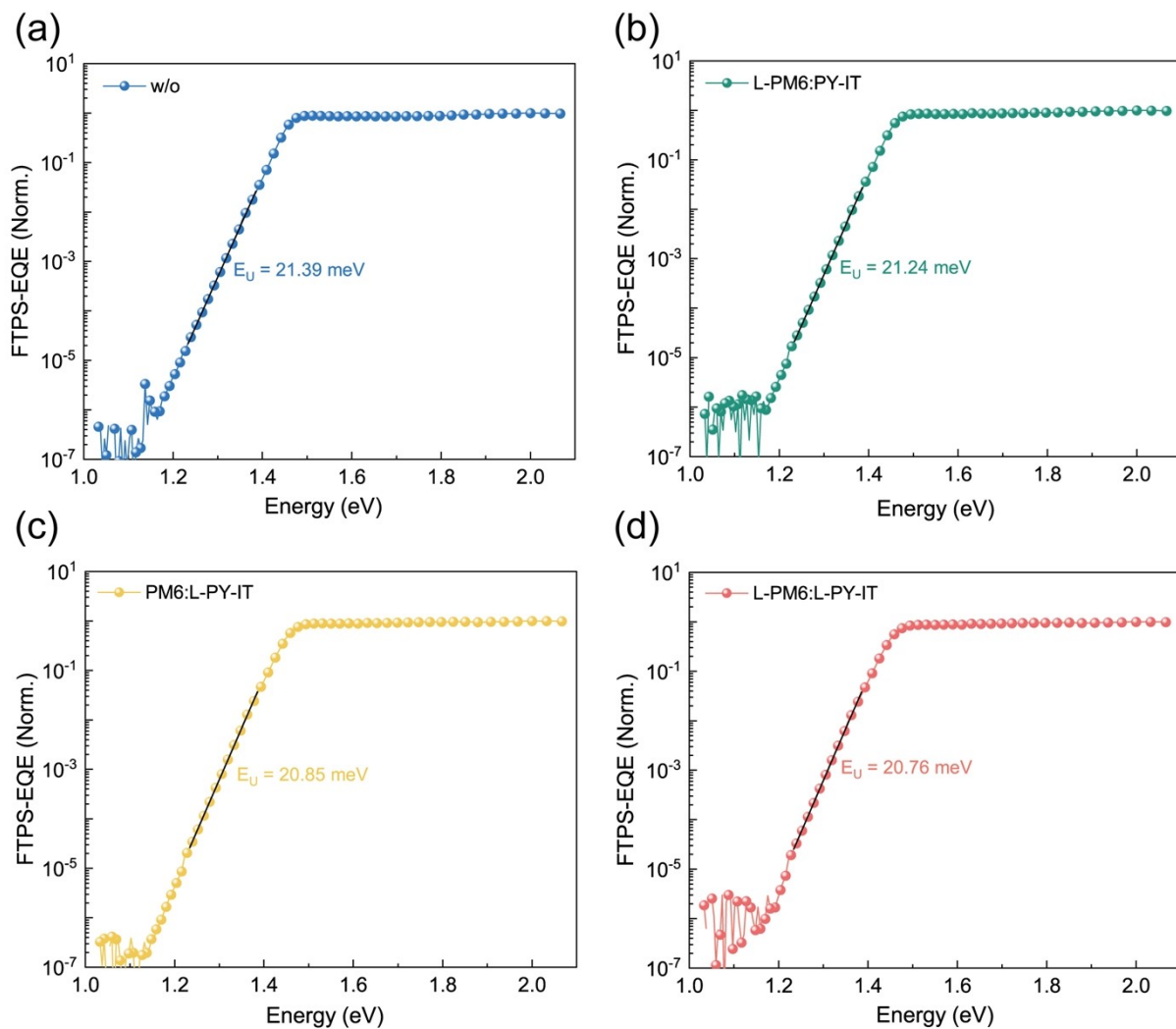


**Fig. S16** FTSP-EQE spectra of (a) w/o, (b) L-PM6:PY-IT, (c) PM6:L-PY-IT, and (d) L-PM6:L-PY-IT devices.

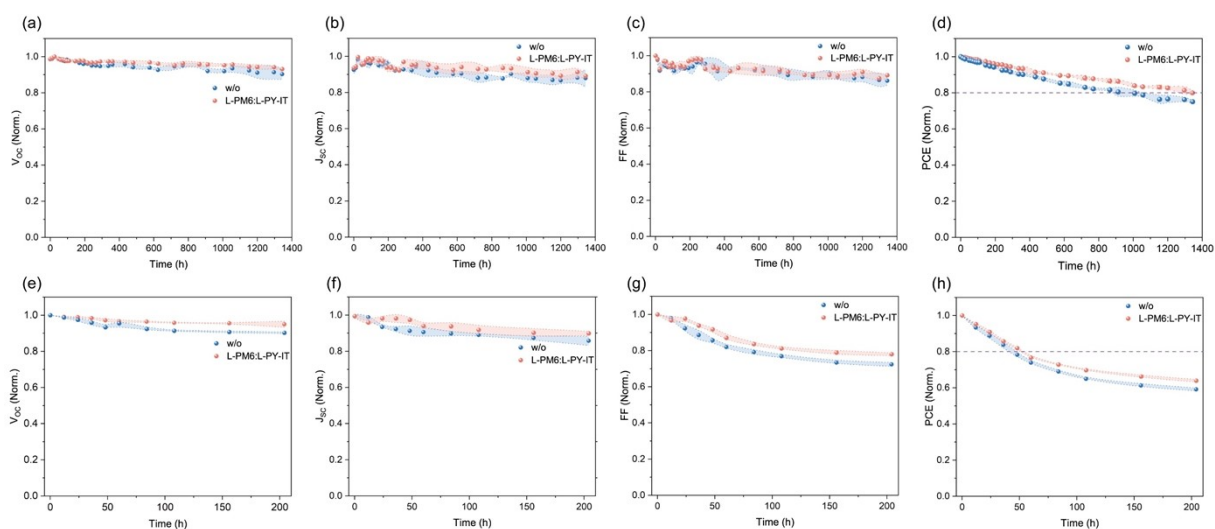


**Fig. S17** Decay of parameters for the (a-d) inverted and (e-f) conventional w/o and L-PM6:L-PY-IT devices under 80 °C thermal stress in N<sub>2</sub> atmosphere.

### 3. Supplementary Tables

**Table S1.** Summary of GIWAXS  $\pi$ - $\pi$  stacking information in the OOP direction of neat films.

Sample	FHWM (nm <sup>-1</sup> )	$q_z$ (Å <sup>-1</sup> )	CCL (nm)	d-spacing (Å)
w/o-PM6	2.704	1.699	2.323	3.699
L-PM6	2.531	1.712	2.483	3.670
w/o-PY-IT	2.688	1.658	2.338	3.790
L-PY-IT	2.444	1.670	2.571	3.763

**Table S2.** Fitting parameters of temperature-related peak position of the PL peaks

Sample	$a$ (meV)	$\Theta$ (K)	$E(0)$ (eV)
w/o-PM6	116.09	1.76	623.80
L-PM6	96.99	1.75	573.90
w/o-PY-IT	116.26	1.35	377.00
L-PY-IT	85.37	1.35	312.70

**Table S3.** Fitting parameters for the pump fluence-dependent TA decay curves.

Sample	$\tau$ (ps)	$k$ ( $\times 10^9$ s <sup>-1</sup> )	$\gamma$ ( $\times 10^9$ cm <sup>3</sup> s <sup>-1</sup> )	$D$ ( $\times 10^{-3}$ cm <sup>2</sup> s <sup>-1</sup> )	$L_D$ (nm)
w/o-PY-IT	656	1.52	5.47	2.18	11.96
L-PY-IT	665	1.5	8.65	3.44	15.12

**Table S4.** Summary of GIWAXS  $\pi$ - $\pi$  stacking information in the OOP direction of different blend films.

<b>Active layer</b>	<b>FHWM (nm<sup>-1</sup>)</b>	<b>q (Å<sup>-1</sup>)</b>	<b>CCL (nm)</b>	<b>d-spacing (Å)</b>
w/o	2.985	1.663	1.89	3.78
L-PM6:PY-IT	2.871	1.680	1.97	3.74
PM6:L-PY-IT	2.796	1.678	2.02	3.75
L-PM6:L-PY-IT	2.687	1.690	2.10	3.72

**Table S5.** Parameters of acceptor localized exciton decay dynamics for different active layers probed at 875 nm.

<b>Active layer</b>	<b>A<sub>1</sub> (%)</b>	<b><math>\tau_1</math> (ps)</b>	<b>A<sub>2</sub> (%)</b>	<b><math>\tau_2</math> (ps)</b>	<b>A<sub>3</sub> (%)</b>	<b><math>\tau_3</math> (ps)</b>	<b><math>\tau_{avg}</math> (ps)</b>
w/o	76.99	0.63	13.55	6.95	9.46	43.64	5.56
L-PM6:PY-IT	58.44	0.20	31.41	1.62	10.15	25.14	3.18
PM6:L-PY-IT	69.84	0.28	20.91	1.72	9.25	21.67	2.56
L-PM6:L-PY-IT	63.98	0.22	26.07	1.52	9.96	18.99	2.43

**Table S6.** Parameters of i-EX decay dynamics for different active layers probed at 1500 nm.

<b>Active layer</b>	<b>A<sub>1</sub> (%)</b>	<b><math>\tau_1</math> (ps)</b>	<b>A<sub>2</sub> (%)</b>	<b><math>\tau_2</math> (ps)</b>	<b>A<sub>3</sub> (%)</b>	<b><math>\tau_3</math> (ps)</b>	<b><math>\tau_{avg}</math> (ps)</b>
w/o	38.40	1.50	28.9	19.32	32.70	716.23	240.35
L-PM6:PY-IT	39.14	1.38	27.09	18.97	33.77	698.41	241.55
PM6:L-PY-IT	44.01	0.87	29.44	26.28	26.54	606.31	169.06
L-PM6:L-PY-IT	41.18	0.54	30.12	15.56	28.70	559.84	165.56

**Table S7.** Parameters of decay dynamics for different active layers probed at 680 nm.

Active layer	$A_1$ (%)	$\tau_1$ (ps)	$A_2$ (%)	$\tau_2$ (ps)	$\tau_{avg}$ (ps)
w/o	65.00	0.81	35.00	3.30	1.68
L-PM6:PY-IT	13.34	0.12	86.66	1.24	1.09
PM6:L-PY-IT	7.13	2.54	92.87	0.63	0.77
L-PM6:L-PY-IT	75.23	0.39	24.77	1.52	0.67

**Table S8.** Rates of these state-to-state transitions derived from the global kinetic model for charge separation of different blend films.

Active layer	$k_1$ (s <sup>-1</sup> )	$k_2$ (s <sup>-1</sup> )	$k_3$ (s <sup>-1</sup> )
w/o	$2.29 \times 10^{12}$	$9.73 \times 10^{10}$	$2.69 \times 10^9$
L-PM6:PY-IT	$2.60 \times 10^{12}$	$1.15 \times 10^{11}$	$3.58 \times 10^9$
PM6:L-PY-IT	$2.52 \times 10^{12}$	$3.09 \times 10^{11}$	$7.66 \times 10^9$
L-PM6:L-PY-IT	$3.96 \times 10^{12}$	$5.09 \times 10^{11}$	$9.63 \times 10^9$

**Table S9.** Lifetimes of states derived from the global kinetic model for charge separation of different blend films.

Active layer	$\tau_1$ (ps)	$\tau_2$ (ps)	$\tau_3$ (ps)
w/o	0.44	10.28	371.35
L-PM6:PY-IT	0.38	8.73	279.70
PM6:L-PY-IT	0.39	3.24	130.62
L-PM6:L-PY-IT	0.25	1.96	103.85

**Table S10.** Carrier mobilities of different devices.

Active layer	$\mu_h^a$ ( $\times 10^{-4} \text{ cm}^2 \text{ V}^{-1} \text{ s}^{-1}$ )	$\mu_e^a$ ( $\times 10^{-4} \text{ cm}^2 \text{ V}^{-1} \text{ s}^{-1}$ )	$\mu_h/\mu_e$
w/o	3.05±0.13	1.71±0.16	1.78
L-PM6:PY-IT	3.28±0.11	1.87±0.19	1.75
PM6:L-PY-IT	3.14±0.15	1.93±0.12	1.63
L-PM6:L-PY-IT	3.36±0.17	2.09±0.14	1.61

<sup>a</sup>The statistical values extracted from ten independent devices.

**Table S11.** Photovoltaic parameters of different devices.

Active layer	$J_{\text{sat}}$ ( $\text{mA cm}^{-2}$ )	$J_{\text{ph}}^*$ ( $\text{mA cm}^{-2}$ )	$J_{\text{ph}}^\#$ ( $\text{mA cm}^{-2}$ )	$P_{\text{diss}}$ (%)	$P_{\text{coll}}$ (%)
w/o	23.81	23.43	20.84	98.40	87.53
L-PM6:PY-IT	24.42	24.05	21.71	98.48	88.90
PM6:L-PY-IT	24.06	23.71	21.62	98.55	89.86
L-PM6:L-PY-IT	24.80	24.46	22.47	98.63	90.60

\*short-circuit condition, #maximal power output condition,  $P_{\text{diss}} = J_{\text{ph}}^*/J_{\text{sat}}$ ,  $P_{\text{coll}} = J_{\text{ph}}^\#/J_{\text{sat}}$ .

**Table S12.** Energy loss parameters of different devices.

Active layer	$J_0^{\text{rad}}$ ( $\text{A m}^{-2}$ )	$qV_{\text{OC}}^{\text{rad}}$ (eV)	$E_g^{\text{PV}}$ (eV)	$qV_{\text{OC}}$ (eV)	$E_{\text{loss}}$ (eV)	$\Delta E_{\text{nonrad}}$ (eV)	$E_U$ (meV)
w/o	$2.411 \times 10^{-17}$	1.130	1.481	0.941	0.540	0.189	21.39
L-PM6:PY-IT	$2.462 \times 10^{-17}$	1.130	1.481	0.942	0.539	0.188	21.24
PM6:L-PY-IT	$2.341 \times 10^{-17}$	1.131	1.481	0.948	0.533	0.183	20.85
L-PM6:L-PY-IT	$2.442 \times 10^{-17}$	1.131	1.481	0.950	0.531	0.181	20.76

**Table S13.** Photovoltaic performance of different inverted devices under simulated AM 1.5 G illumination.

Active layer	$V_{oc}$ (V)	$J_{sc}$ (mA cm <sup>-2</sup> )	FF (%)	PCE <sup>a</sup> (%)
w/o	0.916 (0.911±0.005)	23.50 (23.25±0.25)	72.20 (71.81±0.39)	15.27 (15.21±0.06)
L-PM6:L-PY-IT	0.927 (0.923±0.004)	23.83 (23.65±0.18)	76.16 (75.52±0.64)	16.53 (16.48±0.05)

<sup>a</sup>The statistical values extracted from ten independent devices.

#### 4. Supplementary References

1. B. Fan, X. Du, F. Liu, W. Zhong, L. Ying, R. Xie, X. Tang, K. An, J. Xin, N. Li, W. Ma, C. J. Brabec, F. Huang and Y. Cao, *Nat. Energy*, 2018, **3**, 1051-1058.
2. L. Ye, K. Weng, J. Xu, X. Du, S. Chandrabose, K. Chen, J. Zhou, G. Han, S. Tan, Z. Xie, Y. Yi, N. Li, F. Liu, J. M. Hodgkiss, C. J. Brabec and Y. Sun, *Nat. Commun.*, 2020, **11**, 6005.
3. Y. Wang, D. Qian, Y. Cui, H. Zhang, J. Hou, K. Vandewal, T. Kirchartz and F. Gao, *Adv. Energy Mater.*, 2018, **8**, 1801352.